Characterization of LP133-373: A Double-line, Eclipsing dMe Binary

Undergraduate Research Thesis

Presented in Partial Fulfillment of the Requirements for graduation *with research distinction* in Astronomy & Astrophysics in the undergraduate colleges of The Ohio State University

By

Joseph Schulze

The Ohio State University
May 2017

Project Advisor: Dr. Donald Terndrup, Department of Astronomy

Abstract

Angular momentum loss in stars and star systems can have a significant influence on their evolution. In single stars it causes them to spin down. In multi-star systems it drives the stars inward. This can cause the stars to cease to evolve independently of one another, and, in extreme cases, merge. While the physics of angular momentum loss in stars is poorly understood, it is still possible to measure the rate of loss and probe the mechanisms that drive it. Magnetic stellar winds are one such mechanism in magnetically active stars. The star's winds couple with its magnetic field, and rotate with the star out to large distances carrying away angular momentum. In this study we examine the effects of magnetic stellar winds in the eclipsing low-mass binary system LP133-373. In an eclipsing system, it is possible to quantify the rate of angular momentum loss by measuring the decrease in time between consecutive eclipses. As the system loses angular momentum, and the stars move inward, the time between successive eclipses decreases. To accurately measure orbital period changes due to angular momentum loss in LP133-373, we have more than doubled the number of eclipse timings of this system and increased the monitoring period by over thirteen years. We present observed period changes in LP133-373, derived from our new eclipse timing data, and a comparison calculation of the expected angular momentum loss based on stars of similar masses and rotation periods. Additionally, we present an in-depth characterization of both components of LP133-373. We have obtained over a hundred new spectra of this system allowing us to significantly improve the existing radial velocity solutions, and thus the mass estimates, for both stars.

Table of Contents

List of Tables

List of Figures

Chapter 1: Introduction

Dwarf M (dM) stars are unevolved main sequence stars with masses less than 0.6 solar masses and molecular absorption lines in the visible band of their spectra. Such stars make up over 70 percent of the Galactic stellar population (Henry et al. 1997). Additionally, dM stars provide the best means to detect Earth-like planets in the traditional habitable zone. Since dM stars are cool and dim, the habitable zone exists close to the star. Thus, any potentially habitable planets will orbit near the host star with a short orbital period. Additionally, because of the small masses of these stars, the radial velocity amplitude induced by a planet of a given mass will be larger than that for stars of other spectral types for the same planetary mass. Furthermore, the small orbital distance of habitable planets, coupled with the small masses and radii of dM stars, can allow small terrestrial planets to create a measureable dip in the system's measured brightness as such a planet travels in front of the star relative to an observer's line of sight. A recent example of such systems is the discovery of seven earth-sized planets, three in potentially habitable orbits, around the M dwarf star TRAPPIST-1. However, these low mass stars are still poorly understood, and only a handful of them have been studied in any detail (Birkby et al. 2012).

Currently no model is able to accurately predict many of the observed properties of dM stars. There exists significant disagreement between the theoretically predicted mass-radius relationship of these stars and what is actually observed. The observed radii are 5-10 percent larger than what they are predicted to be for a given mass (Lopez-Morales & Ribas 2005; Ribas 2006; Morales et al. 2010; Torres, Andersen & Giménez 2010; Kraus et al. 2011). One hypothesis to explain this mass-radius anomaly is the presence of significant magnetic activity in M dwarf binary stars (Mullan & MacDonald 2001; Ribas

2006; Torres et al. 2006; Chabrier, Gallardo & Baraffe 2007). This is because many of the studied dM stars are part of dM eclipsing binary systems (MEBs) with short orbital periods, typically less than 2 days (Zahn 1977). In such systems both stars are typically tidally locked to one another causing them to rotate rapidly with one rotation per orbit (so their rotation period is equal to their orbital period).

The mischaracterization of these stars can lead to mischaracterization of any planets orbiting them. The determination of planetary properties, namely, the makeup of their atmospheres, is heavily dependent on the known properties of the host star. Thus, until dM stars are fully understood, and theoretical models properly calibrated in the low mass regime, any planets in orbit around them may be subject to significant mischaracterization (Birkby et al. 2012).

To fully understand and characterize dM stars, it is imperative to study dM stars in eclipsing, double-lined binary systems. Such systems provide the best, model independent way to directly measure fundamental stellar parameters such as mass and radius. Double-lined refers to the fact that in such a system each star's spectrum is individually resolvable. This allows for the extraction of the radial velocities (projection of orbital velocities along observer's line of sight). Since the orbital velocities are directly dependent on the ratio of the masses of the two stars, their masses can be measured from the observed velocities if the inclination angle is known (if it is unknown, you will measure the masses times the cube of the sine of the inclination angle). Eclipsing refers to systems in which the orbital plane of the system nearly edge on as seen from the earth, or in other words the inclination angle, i, is nearly 90°. With this orientation the two components pass in front of one as they orbit causing a dip in the observed brightness. Such systems allow for the direct measurement of the each component's radius and the system's orbital period.

However, only a handful of these low mass binaries, namely those in detached orbits (far enough away from one another that no mass transfer occurs), are well studied. Nine systems were studied and presented in Lopez-Morales & Shaw 2006 and Shaw & Lopez-

Morales 2006. Additional systems have been presented in Bayless & Orosz 2006, Hebb et al. 2006, and Young et al. 2006. Birkby et al. 2012 presents the discovery of sixteen more dM eclipsing binaries systems, and characterizations of three of them. This paper also lists all MEB systems from the literature studied with reasonable precision. The list only contains 18 systems (21 including the three characterized by Birkby et al.), illustrating the need more for more low-mass data.

The focus of our study is the partially eclipsing, double-line dMe binary system LP133-373. Here the e in dMe refers to the fact that emission features are observed in this system. The Luyten 1979 catalog originally listed this system as a red star with a white dwarf making up a common proper motion pair with an angular separation of 5". The system was later found to be a partially eclipsing binary (Rudkin 2003; Oswalt et al. 2005). An initial characterization of this system is presented in Vaccaro et al. 2007. The study finds the system to contain two dM stars with nearly equal masses and radii in a 1.63 day orbital period. However, this study uses just a few radial velocities, and makes numerous simplifying assumptions (this study will be discussed further in Chapter 2.1).

Our study presents an in-depth re-characterization of LP133-373 including a recalculation of the binary parameters and ephemeris, and an examination of eclipse timings to examine period loss due to angular momentum loss in the system via magnetic stellar winds (MSWs). Angular momentum loss in stars and star systems can have a significant influence on their evolution. In single stars it causes them to spin down. In multi-star systems it drives the stars inward. This can cause the stars to cease to evolve independently of one another, and, in extreme cases, merge. While the physics of angular momentum loss in stars is poorly understood, it is still possible to measure the rate of loss and probe the mechanisms that drive it. Magnetic stellar winds are one such mechanism in magnetically active stars. The star's winds couple with its magnetic field, and rotate with the star out to large distances carrying away angular momentum.

In an eclipsing system, such as LP133-373, it is possible to quantify the rate of angular momentum loss by measuring the decrease in time between consecutive eclipses.

As the system loses angular momentum, and the stars move inward, the time between successive eclipses decreases. To accurately measure orbital period changes due to angular momentum loss in LP133-373, we have more than doubled the number of eclipse timings of this system and increased the monitoring period by over thirteen years. We present observed period changes in LP133-373, derived from our new eclipse timing data, and a comparison calculation of the expected angular momentum loss based on stars of similar masses and rotation periods. Additionally, we present an in-depth characterization of both components of LP133-373. We have obtained over a hundred new spectra of this system allowing us to significantly improve the existing radial velocity solutions, and thus the mass estimates, for both stars.

Chapter 2: Data Reduction and Calibration

2.1. Previous Results from the Literature

The most recent study of LP133-373 was done by Vaccaro et al. in 2007. This study presents the modeling of light and velocity curves of LP133-373. They find the system to consist of two nearly identical dM stars in a 1.63 day orbital period each with a mass of $0.340 \pm 0.014\ M_{\odot}$ and a radius of $0.33 \pm 0.02\ R_{\odot}$. However, the study only uses radial velocities at two orbital phases (0.67 and 0.69), seven eclipse timings, and assumes a circular orbit and mass ratio of one. The small radial velocity phase coverage leads to a large uncertainty in the semi-major axis of the orbit, and thus the measured masses. The authors state that a much more complete orbital phase coverage is necessary for a precise characterization of this system. The binary and orbital parameters of LP133-373 found in this preliminary study are shown in Table 2.1.

TABLE 1
LP 133-373 PARAMETERS ($q \equiv 1.0$)

Parameter	Value
T_0	HJD 2452760.70502 ± 0.00013
P (days)	1.6279866 ± 0.0000004
a ($R_\odot$)	5.10 ± 0.22
i (deg)	85.3 ± 0.05
T_1 (K)	3058 ± 195
T_2 (K)	3144 ± 206
$M_{bol,\,1}$	10.0 ± 0.5
$M_{bol,\,2}$	9.8 ± 0.5
Ω_1	16.51 ± 0.12
Ω_2	16.34 ± 0.094
R_1, R_2 ($R_\odot$)	0.330 ± 0.014
M_1, M_2 ($M_\odot$)	0.34 ± 0.02

Table 2.1. Previous characterization results for LP133-373 by Vaccaro et al. 2007. http://iopscience.iop.org/article/10.1086/517872/fulltext/70953.tables.html

2.2. Observations, Reduction, and Calibration

Visible spectroscopy of LP133-373 was obtained between 20 May 2016 and 03 June 2016 using the Ohio State Multi-Object Spectrograph (OSMOS) (Martini et al. 2011) on the Hiltner 2.4-Meter Telescope at the MDM Observatory. Additional visible spectroscopy of the system was also collected during an observing run between 18 June 2016 and 20 June 2016 using KOSMOS (Martini et al. 2014) on the Mayall 4-Meter Telescope at NOAO. In total, over 120 new spectra in the visible band were collected over 20 orbits of LP133-373. The exposure times were 900 seconds and 300 seconds on the Hiltner and Mayall Telescopes, respectively. The image processing followed the standard procedure for overscan correction, sky subtraction, and flattening via flat field exposures. The spectra were extracted using a standard apall procedure in IRAF, which produces a 1D spectrum from a 2D image by averaging over multiple lines across the dispersion axis of the spectrum. The new spectra collected as part of this study have greatly increased the orbital phase coverage of LP133-373 from the initial Vaccaro et al. study as shown in Figure 2.1.

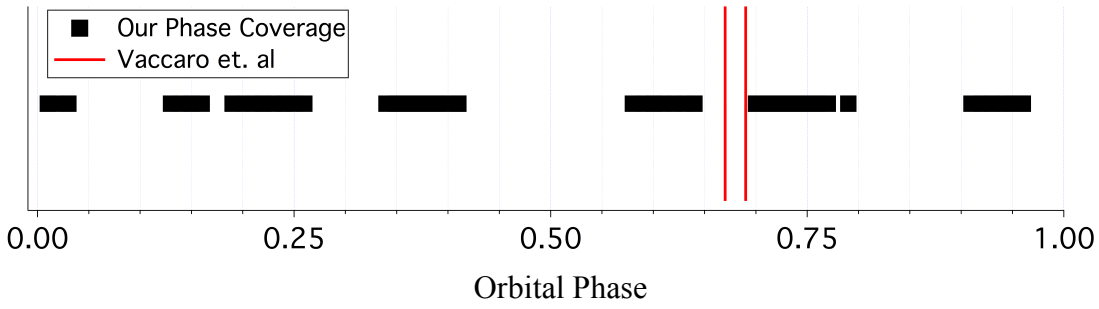

Figure 2.1. New and existing phase coverage of LP133-373.

To calibrate the KOSMOS spectra (from pixel to wavelength) Arc Lamp calibration spectra were collected at numerous positions throughout each observing night. The well-known wavelengths of the Arc Lamp emission lines were used to determine a best-fit polynomial of wavelength as a function of pixel along the dispersion axis of the spectrum. This polynomial not only finds the linear dispersion, but also takes into account non-linear optical mapping effects. Flexure (the physical shifting between the detector and optics as the telescope moves away from zenith) was corrected for by fixing the OI telluric emission line at 5578.39 Å and adjusting all other wavelengths accordingly. The OSMOS spectrograph required a much more sophisticated wavelength calibration procedure, which is the subject of the next section.

Optical photometry of LP133-373 was obtained using the 1.3-Meter McGraw-Hill Telescope at the MDM observatory. The average cadence of the observations is 60.006 seconds, and the exposures were 60 sec in duration. Our new photometric observations have doubled the amount of data and extended the monitoring period of LP133-373 by over thirteen years from the Vaccaro et al. study. Image processing followed the standard overscan correction and flattening procedures.

2.3. Initial OSMOS Wavelength Calibration Model

There are numerous effects that can affect the exact mapping of light onto a detector such as flexure, camera focus, and curvature and tilt of emission lines (due to the exact

way the optics map light onto the detector). If not carefully corrected for these effects can result in incorrectly measured wavelength values, which can lead to line misidentification, or measured radial velocities that differ significantly from the actual values.

The MDM data in this study were taken in a combined program with a radial velocity study of Kepler stars in Cannata 2017. The goal of that work is to detect candidate binary stars by looking for radial velocity variations that indicate the presence of an unseen companion. Both projects require the precise measurement of radial velocities. Thus, it is imperative to understand the mapping of wavelength onto position in the image plane. The OSMOS spectrograph has a complex imaging mapping, and produces curved lines (Figure 2.2), which means that the wavelengths depend on the Y location. In other words two spectra take at different Y locations will have different wavelength solutions. The telescope focus is sensitive to temperature; this results in spectra taken at different temperature having different zero point and dispersion, and even different higher order terms. So while we took frequent arc spectra to help map out these effects, we did not take an arc spectrum for each and every object in order to maximize observing time, instead hoping that the behavior of the instrument would be regular enough that we could model everything.

In order to understand the exact magnitude of these various effects, the line positions of various arc lamps were measured as a function of x position, y position, and camera focus. In doing this, the effects of curvature and tilt (Figure 2.2) and camera focus (Figure 2.3), were found to be drastic enough to require sophisticated modeling in order to reproduce the positions of the arc line locations at zenith and reach the needed precision desired for this study of LP133-373.

The peak location of a single emission line was observed to differ by up to 4 pixels due to differing camera focuses during the observing run. On the red end of the detector (near H-alpha) the difference in peak pixel locations for a single line can be as much as 4

pixels, which corresponds to a Doppler shifted velocity of roughly 130 km/s. Curvature and tilt were observed to create a shift of up to 3 pixels on the red end corresponding to a radial velocity of roughly 100 km/s. These velocity shifts are very near the expected velocity amplitude of LP133-373, and thus it is imperative that these effects are properly calibrated.

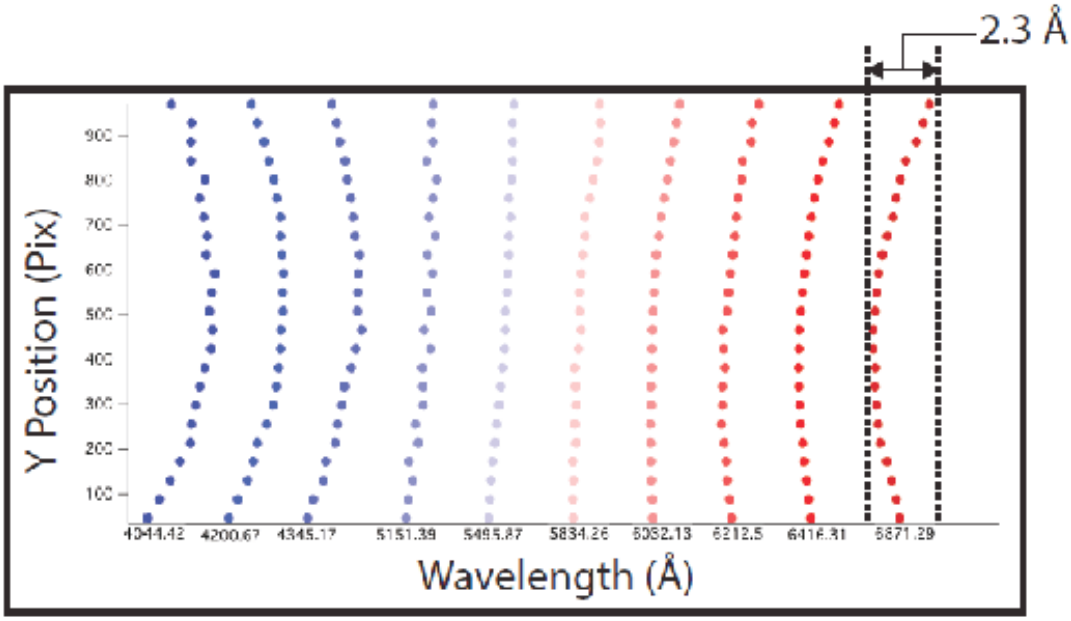

Figure 2.2. Effects of curvature and tilt on emission lines of the Argon Arc Lamp. These effects can be as large as 2.3 angstroms near the location of the Hydrogen-Alpha line corresponding to a Doppler shifted velocity of roughly 100 km/s.

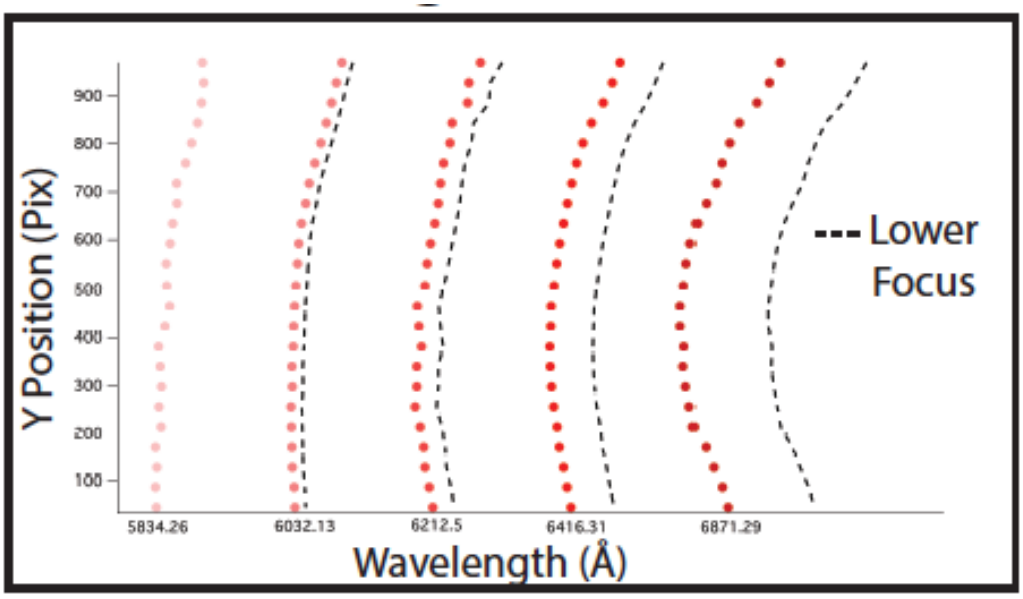

Figure 2.3. Effect of camera focus on the red end of the OSMOS detector (near the Hydrogen-Alpha line). Here this effect can produce a difference of up to 4 pixels on this end of the detector between spectrum corresponding to a Doppler shifted velocity near 130 km/s.

The standard calibration procedure, and the one used on the spectra obtained with KOSMOS (as discussed in 2.2.), is to fit a polynomial function of x, such as

$$W = a_0 + a_1 x + a_2 x^2 + a_3 x^3 + a_4 x^4 \tag{3.1}$$

to a line across an arc lamp spectrum at the same y location as the object spectrum that is being calibrated. If there exists a calibration spectrum taken at the same hour angle with the same parameters (namely camera focus) as the object spectrum, then this approach is sufficient. However, this was not the case for many of the spectra collected at MDM, and a full hierarchical model of the detector was necessary.

Due to the effects tilt and curvature, it was found that the zero term, a_0, the dispersion term, a_1, and the quadratic term, a_2 are all dependent on y (this can be visually seen in Figure 2.2). The offset coefficient, and dispersion terms are quadratic functions of y

$$a_0 = z_0 + z_1 y + z_2 y^2 \tag{3.2}$$

and

$$a_1 = d_0 + d_1 y + d_2 y^2. \tag{3.3}$$

The quadratic coefficient was found to be a linear function of y

$$a_2 = q_0 + q_1 y. \tag{3.4}$$

In this model, the coefficients were made to be deterministic functions of the above equations, in that they are completely determined by the values of their function coefficients.

Finally it was found that the zero coefficients z_0 and d_0 I were linear functions of the camera focus (this can be seen in Figure 2.3)

$$z_0 = f_0 + f_1 F \tag{3.5}$$

and

$$d_0 = p_0 + p_1 F. \tag{3.6}$$

Where F is the camera focus in microns. Thus the zero wavelength and dispersion coefficient depend not only on y location, but also have a nested dependence on the camera focus. Using this hierarchal modeling we were able to reproduce the location of the lines of an Argon arc lamp at the zenith with a residual scattering of 0.09 angstroms, or roughly 3 km/s near the H-alpha line. The values determined for each coefficient are shown in Table 2.2, and the model residuals are shown in Figure 2.4.

Coefficient	Mean Coefficient Value	Standard Deviation	Units
f0	6.86E+03	2.05E-02	Å
f1	4.16E-03	3.58E-06	$Å*\mu m^{-2}$
z1	4.39E-03	3.79E-05	$Å*Pix^{-1}$
z2	-5.30E-06	3.47E-08	$Å*Pix^{-2}$
p0	-7.02E-01	9.91E-06	Å
p1	-3.62E-06	1.70E-09	$Å*\mu m^{-1}$
d1	-2.98E-06	2.26E-08	$Å*Pix^{-2}$
d2	2.97E-09	1.68E-11	$Å*Pix^{-3}$
q0	-1.42E-05	4.09E-09	$Å*Pix^{-2}$
q1	9.62E-12	3.16E-12	$Å*Pix^{-3}$
a3	3.50E-09	6.66E-13	$Å*Pix^{-3}$
a4	7.69E-14	2.13E-16	$Å*Pix^{-4}$

Table 2.2. Coefficient values for OSMOS wavelength calibration model. The coefficients a_0, a_1, a_2, z_0, and d_0 are not included because they are fully determined via (3.2), (3.3), (3.4), (3.5), and (3.6) respectively.

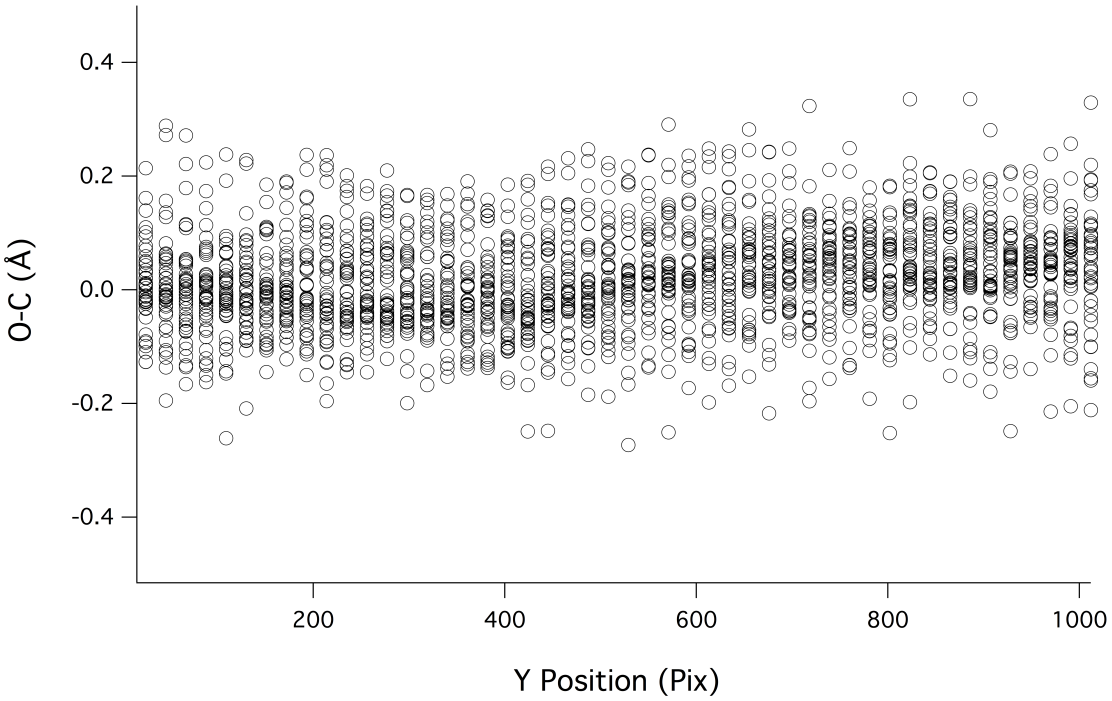

Figure 2.4. OSMOS calibration model residuals. The residuals are plotted as a function of Y position for the model applied to an Argon lamp spectrum taken on the night of 20160518. The rms of the residuals is about 0.09 Å.

In addition to curvature and tilt, another large effect that needs to be corrected for is flexure. This effect was observed to produce a shift of up to two pixels over the course of a single night, which corresponds to a velocity of near 80 km s^{-1}. However, it is well behaved, and has an approximately linear dependence on hour angle (the pointing angle of the telescope relative to the zenith). Fitting this effect to a linear function on a given night yields residuals between about 0.08-0.10 pixels, or around 2-4 km s^{-1} near H-alpha. With all of the effects corrected for, we were able to reproduce the radial velocities of radial velocity standards with a standard deviation of roughly 10 km s^{-1} in Cannata 2017.

Chapter 3: Radial Velocity Extraction and Analysis

3.1. Extraction of Stellar Masses in a Double-line Binary

Here, I present a condensed explanation of the basic physics behind the extraction of the masses of both components of a double-line binary in a circular orbit (see An Introduction Modern Stellar Astrophysics by Ostlie and Carroll for full derivation). In these systems, where the emission lines of both components are resolved, it is possible to measure the Doppler shift in these emission lines, and thus their radial velocities since

$$v = \frac{\Delta\lambda}{\lambda} \mathrm{c} \tag{3.1}$$

(for v<<c as is the case with LP133-373). $\Delta\lambda$ is the difference between the measured wavelength of an emission or absorption feature and the known, rest wavelength, and λ is the known wavelength.

If one extracts the radial velocities, and plots them as a function of phase a sinusoidal behavior is observed (see Figure 3.1). The ratio of amplitudes of the curve for each star is directly determined from the ratio of their masses

$$\frac{v_{r2}}{v_{r1}} = \frac{m_1}{m_2} . \tag{3.2}$$

where m_1 is the mass of the primary component, m_2 is the mass of the secondary, vr_1 is the radial velocity of the primary, and vr_2 is the radial velocity of the secondary.

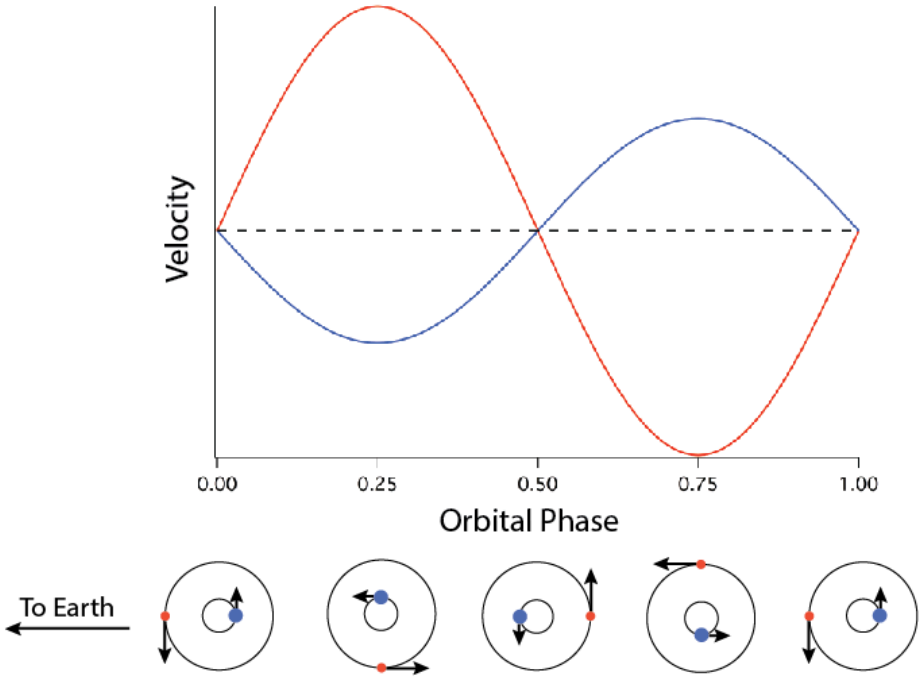

Figure 3.1. Artificial velocity curve for a binary system. Here both components are in circular orbits but have different masses. Orbital phases 0.0 and 1.0 correspond to primary eclipses. Orbital phase 0.5 corresponds to a secondary eclipse. Phases 0.25 and 0.75 correspond to quadrature (maximum separation relative to the line of sight). Blue and red indicate the primary and secondary components, respectively. The black arrows give the direction of each star's orbital velocities.

Solving Kepler's third law for the sum of the masses, and using the fact that $v_r = v \sin i$ (where v_r is the radial velocity, v is the actual orbital velocity, and i is the inclination angle), to rewrite the actual orbital velocities in terms of the observed radial velocities leads to

$$m_1 + m_2 = \frac{P}{2\pi G} \frac{(v_{1r}+v_{2r})^3}{\sin^3 i} . \tag{3.3}$$

Where P is the orbital period, and G is the gravitational constant. Thus if the period (which can be measured via eclipse timings in eclipsing binaries like LP133-373) and inclination angle are known, and the radial velocity amplitudes are measureable then the combination of equations (3.2) and (3.3) provides a direct means to calculate the mass of each component. Solving the two equations for m_1 and m_2 gives

$$m_1 = \left(1 + \frac{v_{r1}}{v_{r2}}\right)^{-1} \frac{P}{2\pi G} \frac{(v_{r1}+v_{r2})^3}{\sin^3 i} \tag{3.4}$$

and

$$m_2 = \left(1 + \frac{v_{r2}}{v_{r1}}\right)^{-1} \frac{P}{2\pi G} \frac{(v_{r1}+v_{r2})^3}{\sin^3 i} . \tag{3.5}$$

3.2 Extraction of LP133-373 Radial Velocities

Radial velocities for LP133-373 were extracted using the H-alpha emission line. The H-alpha lines from each star were decomposed by modeling the composite profile as a sum of two Gaussian peaks (see Figure 3.2d). For now, this study limits itself to using spectra taken near quadrature (phase = 0.25 and 0.75), since the H-alpha emission lines are only resolvable in this system near quadrature as the velocity amplitudes are only slightly larger than the spectral resolution of the detectors. We are currently developing a more sophisticated modeling technique that will allow us to de-blend unresolved lines. The extracted radial velocities are shown in Table 3.1.

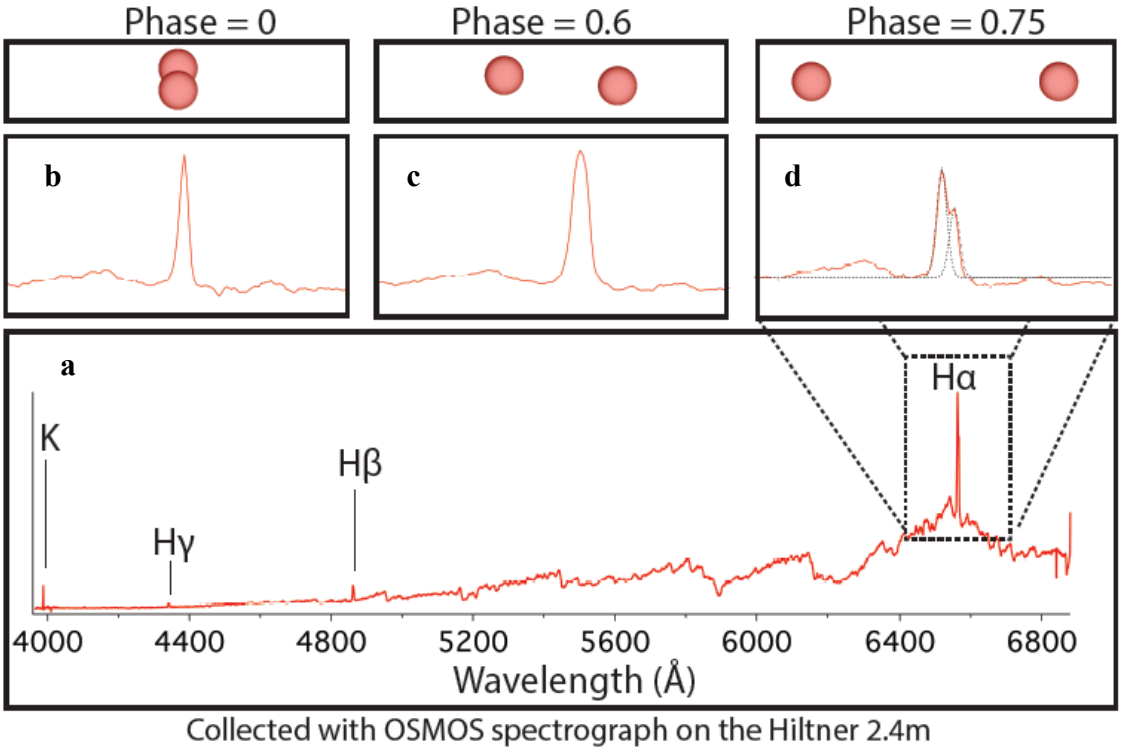

Figure 3.2. LP133-373 spectrum in the visible band. 1a shows a full LP133-373 spectrum. 1b shows the H-alpha emission line near phase zero. 1d shows H-alpha near quadrature. The lines are seen to be resolved as is characteristic of a double-line binary. 1c shows an intermediate phase where the individual components are not resolved but the profile is broader than at eclipse.

3.3 Mass Measurement of Both LP133-373 Components

To obtain a preliminary estimate of the masses of both components of the LP133-373 system, the radial velocities were extracted from the KPNO spectra near quadrature, and plotted as a function of orbital phase. The resultant curves were then simultaneously fit to the radial velocity equation for a circular orbit (e = 0)

$$RV = v_0 + A\sin(2\pi * Phase). \tag{3.6}$$

In (3.6) v_0 is the systemic velocity of the center of mass of the system. This coefficient was linked during the fitting so that it was the same for both components (as it must be). The coefficient A is the radial velocity amplitude, which is the coefficient needed to find the masses of each star. This raw data and fit, along with the residuals are shown in Figure 3.3. A systemic velocity of -34.5 ± 0.5 km s^{-1}, radial velocity amplitude for the primary component of 73.2 ± 0.7 km s^{-1}, and radial velocity amplitude for the secondary of 82.6 ± 0.7 km s^{-1} were obtained. The radial velocity data used in Figure 3.3 is listed in Table 3.1.

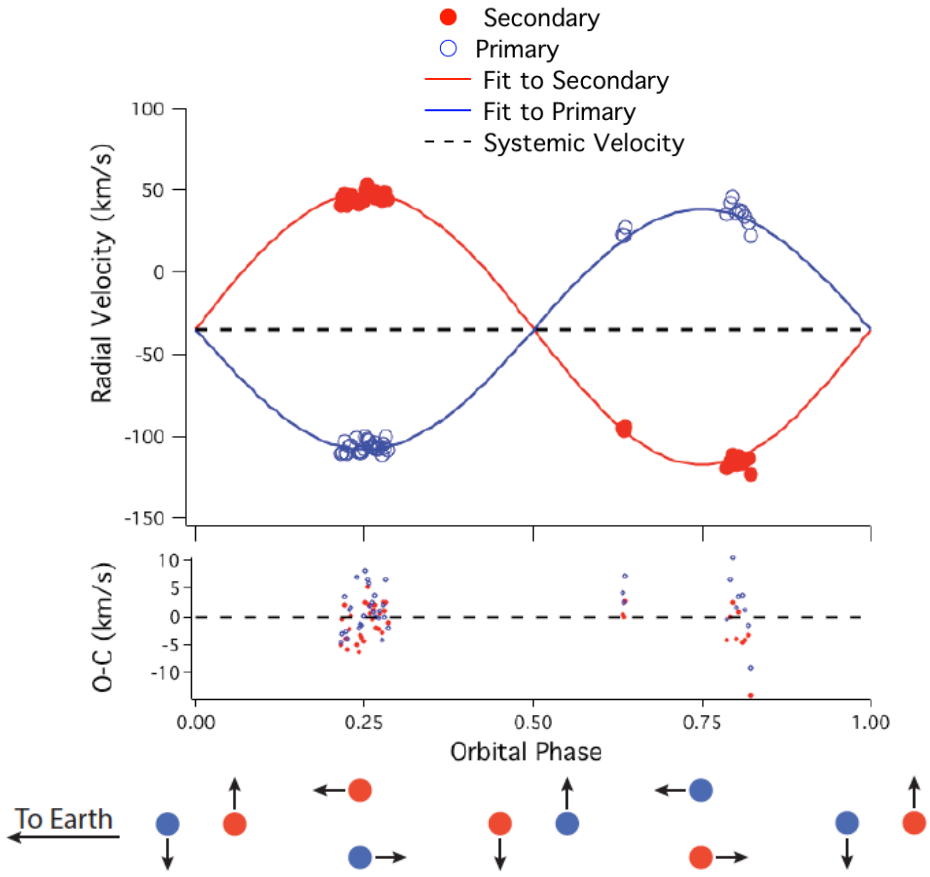

Figure 3.3. LP133-373 radial velocity curves. Radial velocity measurements for each component of LP133-373 collected with the 4-Meter Mayall Telescope, along with fits and residuals. The rms of the residuals are 4.2 and 3.8 km s^{-1} for the primary and secondary fits, respectively.

The extracted radial velocities, and the values for the orbital period and inclination angle from Vaccaro et al. were then used in Equations (3.4) and (3.5) to calculate the masses of both components of LP133-373. The mass of the primary component was found to be $0.342 \pm 0.003\ \mathrm{M}_{\odot}$. The mass of the secondary was found to be $0.303 \pm 0.003\ \mathrm{M}_{\odot}$. This yields a mass ratio of 1.13, which is 13% larger than the mass ratio assumed in Vaccaro et al.

The quoted mass errors were obtained via the standard propagation of uncertainty for a general function. The exact formula used was

$$\delta M = \sqrt{\left(\frac{\partial M}{\partial v_{r1}}\delta v_{r1}\right)^2 + \left(\frac{\partial M}{\partial v_{r2}}\delta v_{r2}\right)^2 + \left(\frac{\partial M}{\partial P}\delta P\right)^2 + \left(\frac{\partial M}{\partial i}\delta i\right)^2}. \tag{3.7}$$

The mass formulas used for *M* are given via Equations 3.4 and 3.5. The errors listed in Table 2.1 from Vaccaro et al. were used for the period and inclination angle uncertainties.

While the procedure outlined in this section gives a sufficient first order estimate of the masses of both components of LP133-373, and the residuals in Figure 3.3 suggest the orbit is very nearly circular, we still plan to do a more sophisticated modeling of the radial velocity curves that allows for a non-zero eccentricity. This will allow us to better characterize the orbit, and ultimately determine the masses even more precisely.

Orbital Phase	RV Secondary (km s^{-1})	RV Primary (km s^{-1})
0.21511	40.7	-110.9
0.21769	45.6	-109.7
0.22006	48.3	-103.3
0.22246	42.6	-109.6
0.22479	40.8	-111.0
0.22713	44.7	-106.1
0.22946	47.2	-105.8

0.23879	42.5	-101.0
0.24177	41.3	-109.9
0.24422	44.4	-109.3
0.24665	44.0	-109.7
0.24955	43.4	-108.0
0.25190	50.3	-100.1
0.25423	53.0	-101.5
0.25658	49.8	-102.2
0.25897	48.2	-106.2
0.26134	47.0	-105.3
0.26367	48.7	-107.0
0.26604	49.3	-104.0
0.26838	45.1	-107.7
0.27073	44.8	-107.7
0.27330	47.4	-106.2
0.27566	43.8	-111.2
0.27800	48.9	-104.9
0.28034	47.3	-106.9
0.28270	48.5	-100.0
0.28503	44.6	-108.2
0.63147	-95.3	23.1
0.63380	-96.4	22.2
0.63613	-94.6	27.6
0.78664	-119.4	35.8
0.79111	-114.9	42.4
0.79557	-111.7	45.7
0.80004	-117.4	36.4
0.80450	-112.0	37.7
0.80897	-116.5	37.2
0.81341	-115.1	33.8
0.81787	-113.4	30.3
0.82232	-123.0	21.8

Table 3.1. LP133-373 radial velocities obtained with the 4-Meter Mayall Telescope.

Chapter 4: Eclipse Timings and Period Analysis

4.1. Measuring the Orbital Period in an Eclipsing Binary

In an eclipsing system it is possible to directly measure the orbital period of the system. This is typically accomplished by measuring the time between two consecutive primary eclipses (although it is also possible to use secondary eclipses), where the eclipse time is defined as the time of mid-eclipse (when the maximum amount of light is blocked during a single eclipse). A primary eclipse is defined as the eclipse that results in the largest decrease in the measured light, and the secondary eclipse is the one that results in a lesser decrease. Since LP133-373 consists of two very similar stars, the resultant primary and secondary eclipses of this system are nearly identical. An example light curve is shown in Figure 4.1 along with the definition of the orbital period being used here.

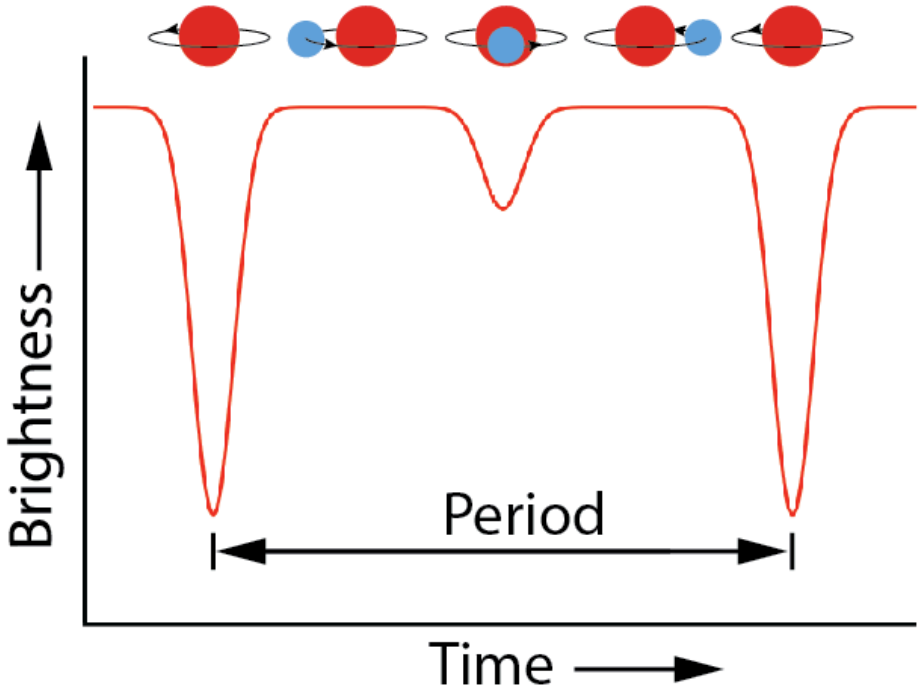

Figure 4.1. Artificial light curve of a partially eclipsing binary over one orbital period. The time between consecutive eclipses gives the orbital period.

In a static system, if both the orbital period and a reference epoch, T_0 (some zero time when an eclipse was known to occur) are known, one can build a linear ephemeris that gives the time of the nth eclipse since T_0,

$$T = T_0 + Period * n. \tag{4.1}$$

While a linear ephemeris is often sufficient, and usually provides an excellent starting approximation, namely when calculating T for small n, there are often physical mechanisms that can change the period. In such cases higher order terms are necessary to create an ephemeris that can accurately predict eclipse timings for a large number of eclipses. Some examples of non-linear effects are apsidal motion, the presence of a third body, or changes in the angular momentum of the system. Vaccaro et al. calculates the following linear ephemeris for LP133-373

$$T = 2{,}452{,}760.70502 \pm 0.00013 + (1.6279866 \pm 0.0000004) * n, \quad (4.2)$$

where the initial epoch is given as a HJD, and the period is in days. The study claims to find no significant period changes in the system. In this chapter, we present a new ephemeris calculation of LP133-373, and reanalyze the system for any period changes, namely for period loss due to magnetic stellar winds.

4.2 New Eclipse Timings of LP133-373

In this section we present the measurement of three new eclipse timings of LP133-373. The eclipse times were measured by finding the centroid of the eclipse. In other words we measured the time at which the received light was a minimum. Figure 4.2 and 4.3 show two example light curves of LP133-373 collected as part of this study. The three new eclipse timings measured from the light curves of LP133-373 are given in Table 4.2.

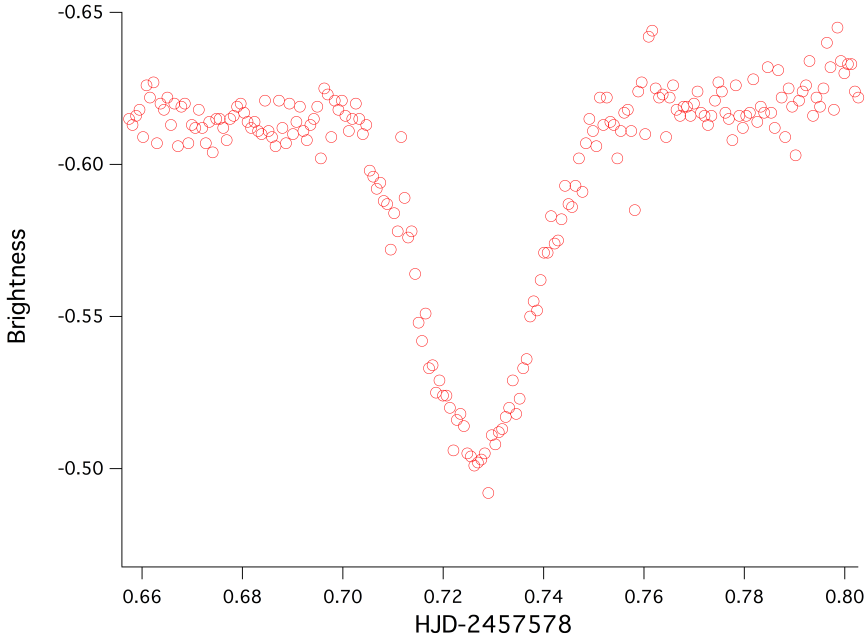

Figure 4.2. LP133-373 light curve. The vertical axis is the brightness of LP133-373 relative to a weighted average of seven comparison stars. The more negative the brightness, the brighter LP133-373 is relative to the comparison stars.

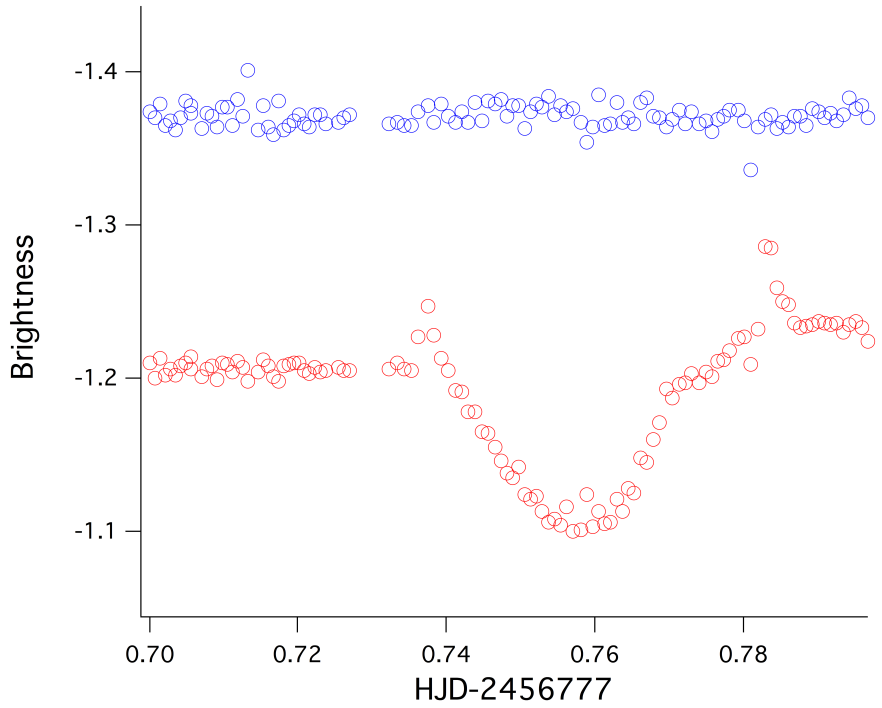

Figure 4.3. LP133-373 light curve with flaring. The light curve of LP133-373 is shown with open, red circles. The open, blue circles give the brightness of a single comparison relative to the other comparison stars with an artificial offset. All comparison stars exhibited the same steady behavior indicating that the flaring that can be seen before and after the eclipse is a real feature in the LP133-373 light curve.

We are currently still working on the analysis of our new photometric observations, and thus the three eclipse timings given in this section only make up about half of the available eclipse timing data we will eventually use to calculate the period and any period loss in this system.

4.3 New Orbital Period Measurement of LP133-373

In this section, we present a new preliminary calculation of the orbital period of LP133-373 using our three new eclipse timings, and an observed period change. These three timings were fit to a linear ephemeris, using the same zero epoch as Vaccaro et al.

Our newly measured period, and the period measured in Vaccaro et al. are shown along with their errors in Table 4.1. Additionally the eclipse timings used in our period calculation are shown in Table 4.2, along with their corresponding eclipse numbers, residuals with respect to our new linear ephemeris, and the measured shifts from the expected timings of these eclipses using the original Vaccaro et al. ephemeris.

	Period (days)	Error (days)
Vaccaro et al.	1.6279866	0.0000004
New Period Calculation	1.62798509	0.000000029

Table 4.1. Calculated periods for LP133-373. We observe a slight decrease in the orbital period of LP133-373 with respect to the Vaccaro et al. period.

Date (UT)	Eclipse Center (HJD)	Eclipse Number	O-C (s)	Shift (s)
20130619	2456462.74387602	2274.0	60.2	-230.9
20140429	2456777.75768281	2467.5	-52.9	-369.2
20160709	2457578.72693591	2959.5	-2.1	-382.5

Table 4.2. New eclipse timings of LP133-373. The first column is the date of observation given in universal time. The second is the time of the center of the eclipse (maximum decrease in observed brightness) in HJD. The third column is the corresponding eclipse number (0.5 indicates the eclipse is a secondary eclipse), *n*, based off of the Vaccaro et al. Ephemeris. The fourth column gives the residuals calculated using our newly calculated period. The last column gives the difference between our measured eclipse times, and the calculated eclipse times from the Vaccaro et al. ephemeris.

4.4 Preliminary Analysis of Period Loss in LP133-373

The period calculation presented in section 4.3 shows a decrease in the orbital period of LP133-373 suggesting angular momentum loss in the system due to magnetic stellar winds. In this section, a calculation of the magnitude of period loss is presented.

To calculate the magnitude of period change in LP133-373 our newly measured eclipse timings (given in Table 4.3) were fit to a second order polynomial

$$T = T_0 + P_0\, n + \frac{1}{2}\dot{P}\, n^2 \tag{4.3}$$

via a least squares fit. The zero epoch, T_0, and period, P_0, were held fixed using the values from Vaccaro et al. $\dot{P}$ can be seen to be the change in the orbital period per eclipse by differentiating (4.3) with respect to n. Differentiating (4.3) gives the rate of change of the eclipse time, T,

$$\frac{dT}{dn} = P_0 + \dot{P}\, n. \tag{4.4}$$

The term on the right hand side is just the period of the system at some eclipse number. For a linear ephemeris the rate of change is just the constant initial orbital period P_0. However, when non-linear effects are present the period changes by some amount $\dot{P}$ per orbit. Via a least squares fit, the value for this period change coefficient was found to be

$$-9.67 * 10^{-5} \pm 1.47 * 10^{-5} \text{ s n}^{-1}.$$

Some relevant values from the results of this fit are given in Table 4.4.

Eclipse Number	Expected T (HJD)	Calculated T from Fit (HJD)	Residuals (s)	$\dot{P} * n\ (s)$
2274.0	2456462.74655	2456462.74366	-19.02669	0.22
2467.5	2456777.76196	2456777.75855	74.89788	0.24
2959.5	2457578.73136	2457578.72646	-40.83422	0.29

Table 4.3. Values from polynomial fit to new eclipse timings. The first column gives the eclipse number, *n*. The second column gives the expected eclipse time in HJD using the linear ephemeris calculated by Vaccaro et al. The third column gives the calculated eclipse times in HJD using the polynomial fit. The fourth column gives the difference (O-C) of the newly observed eclipse timings and the calculated ones from the second column. The fifth column gives the period decrease after n eclipses in seconds calculated by multiplying $\dot{P}$ by the eclipse number.

Propagating the error in the period from the Vaccaro et al. ephemeris to our last measured eclipse leads to an uncertainty of 102.3 seconds. This uncertainty in the period is significantly larger than the changes in the period due to the determined period loss coefficient, $\dot{P}$ (last column in Table 4.3). Thus it is possible that the period change that has been observed is due to the uncertainty in the period over an extended monitoring period. It is also possible that the measure period change coefficient is due to some other physical mechanism such as apsidal motion (this will be discussed in more detail in 5.2). Thus additional analysis is needed to reach a more decisive conclusion. More specifically, better modeling of light curves especially when the system is flaring, and additional eclipse timings are necessary to better our analysis.

Chapter 5: Conclusions and Future Work

5.1 Conclusions

In this study we have presented significant new spectroscopic and photometric observations of the double-line, partially eclipsing dMe binary system LP133-373. Using spectra collected near quadrature with KOSMOS on the 4m Mayall Telescope we measured the radial velocities of both components of LP133-373. Assuming a circular orbit, radial velocity analysis yielded a primary component mass of LP133-373 to have a mass of $0.342 \pm 0.003\ M_{\odot}$ and a secondary mass of $0.303 \pm 0.003\ M_{\odot}$ yielding a mass ratio of 1.1, which is larger than the preliminary mass ratio found in Vaccaro et al.

Next, using our new photometric observations we presented three new eclipse timings. Using these eclipse timings we recalculated the orbital period of LP133-373 using a linear ephemeris model, and found it to be $1.62798509 \pm 0.000000029$ days, which is smaller than the original period found in Vaccaro et al., suggesting a period loss due to magnetic stellar winds. We then allowed for a period loss parameter in our model, and found evidence of a period change; however, further analysis with more data and better light curve modeling is needed to determine the exact cause.

5.2 Future Work

While our preliminary radial velocity analysis has already done much to increase the knowledge of the masses of both components of LP133-373, we still have a significant amount of data over a larger number of phases to include in our analysis. We are currently working on calibrating the OSMOS spectra using the calibration model discussed in section 2.3. Additionally, we are working on modeling the unresolved H-alpha emission lines of LP133-373. Once we have extracted the radial velocities collected from the OSMOS spectra, and extracted all of the radial velocities of LP133-373 at unresolved phases, we will have much more complete radial velocity curves of both components. Furthermore, we intend to do a more general modeling of the radial velocity curves with additional orbital parameters such as eccentricity. This increased phase coverage and better modeling will allow us to measure the masses even more precisely, look for third bodies, and further understand the orientation and orbital shape of the system.

We also plan to do a more sophisticated modeling of the LP133-373 light curves we have already analyzed in this study, and model additional ones. This will allow us to better calculate the period, and look for any period changes due to angular momentum loss via MSW's. Despite our initial conclusion of no significant period change, if this system does indeed show signs of period change we will need to be careful to make sure we understand the exact mechanism causing these changes. In addition to magnetic stellar winds there are various other effects such as apsidal motion, or a third body, that can manifest themselves as a period change.

Apsidal motion, or apsidal precession, is simply the precession of the orbit of a two bodies. This effect causes a sinusoidal variation in both the primary and secondary eclipse timings (see Hong et al. 2016). Over short time intervals (relative to the period of this effect), the eclipse timing variations look linear. Similarly, the presence of an unseen third body present will cause the orbit of the two primary components to move around

with a period equal to that of the third body's, leading to sinusoidal variations in the eclipse timings. Since angular momentum loss causes the eclipse timings of both the primary and secondary eclipses to continuously decrease, we will need to look at the period change of both types of eclipses in LP133-373 to sufficiently differentiate between these various effects, and determine whether there is any indication of period loss via magnetic stellar winds.

Additionally, by measuring the time it takes for an eclipsing system to go into and out of eclipse and the eclipse depths, it is possible to measure the radii of both components. Thus, better light curve modeling will also allow us to measure the radii of both components of LP133-373.

References

Bayless, A. J., & Orosz, J. A. 2006, ApJ, 651, 1155

Birkby, J., Nefs, B., Hodgkin, S., et al. 2012, MNRAS, 426, 1507

Chabrier G., Gallardo J., Baraffe I., 2007, A&A, 472, L17

Cannata et al. 2017, Undergraduate Honors Thesis, The Ohio State University

Hebb, L., Wyse, R. F. G., Gilmore, G., & Holtzman, J. 2006, AJ, 131, 555

Henry T. J., Ianna P. A., Kirkpatrick J. D., Jahreiss H., 1997, AJ, 114, 388 Hewett P. C., Warren S. J., Leggett S. K., Hodgkin S. T., 2006, MNRAS, 367, 454

Hong, K., Lee, J. W., Kim, S.-L., et al. 2016, MNRAS, 460, 650

Lopez-Morales M., Ribas I., 2005, ApJ, 631, 1120

Lopez-Morales, M., & Shaw, J. S. 2006, preprint (astro-ph/0603748)

Luyten, W. J. 1979, A Catalogue of Stars with Proper Motions Exceeding 0.500 Annually (2nd ed; Minneapolis: Univ. Minnesota)

Paul Martini et al. 2011, PASP, 123, 187

Martini P., Elias J., Points S. et al., "KOSMOS and COSMOS: New facility instruments for the NOAO 4-meter telescopes," Proc. SPIE 9147 91470Z, (2014)

Morales J. C., Gallardo J., Ribas I., Jordi C., Baraffe I., Chabrier G., 2010, ApJ, 718, 502

Oswalt, T. D., Rudkin, M., Johnston, K., Kissinger, J., & Menezes, K. 2005, in ASP Conf. Ser. 334, 14th EuropeanWorkshop on White Dwarfs, ed. D. Koester & S. Moehler (San Francisco: ASP), 605

Ribas I., 2006, Ap&SS, 304, 89

Rudkin, M. 2003, M.S. thesis, Florida Institute of Technology

Shaw, J. S., & Lopez-Morales, M. 2006, preprint (astro-ph/0603744)

Torres G., Andersen J., Giménez A., 2010, A&AR, 18, 67

Young, T. B., Hidas, M. G., Webb, J. K., Ashley, M. C. B., Christiansen, J. L., Derekas, A., & Nutto, C. 2006, MNRAS, 370, 1529

Zahn J., 1977, A&A, 57, 383

Acknowledgements

I would thank Dr. Terndrup for his continued oversight and much appreciated counsel on this project and my development into an independent researcher since I began working with him in May 2016. I would also like to thank Grace Calhoun and Rachel Cannata for helping with the collection of data used in this study. Finally, I would like to thank Dillon Sanders for his contributions to the light curve modeling techniques used for the eclipse timings of LP133-373.